The Journal of Chemical Physics

Photodissociation dynamics of N_3^+

Cite as: J. Chem. Phys. **156**, 124307 (2022); https://doi.org/10.1063/5.0085081
Submitted: 12 January 2022 • Accepted: 01 March 2022 • Accepted Manuscript Online: 02 March 2022 • Published Online: 25 March 2022

Sarbani Patra, Juan Carlos San Vicente Veliz, Debasish Koner, et al.

The Journal of Chemical Physics ARTICLE scitation.org/journal/jcp

Photodissociation dynamics of N_3^+

Cite as: J. Chem. Phys. 156, 124307 (2022); doi: 10.1063/5.0085081
Submitted: 12 January 2022 • Accepted: 1 March 2022 •
Published Online: 25 March 2022

View Online Export Citation CrossMark

Sarbani Patra,[1] Juan Carlos San Vicente Veliz,[1] Debasish Koner,[1,2] Evan J. Bieske,[3] and Markus Meuwly[1,a)]

AFFILIATIONS

[1] Department of Chemistry, University of Basel, Klingelbergstrasse 80, CH-4056 Basel, Switzerland
[2] Department of Chemistry, Indian Institute of Science Education and Research (IISER) Tirupati, Karakambadi Road, Mangalam, Tirupati 517507, Andhra Pradesh, India
[3] Department of Chemistry, University of Melbourne, Parkville 3010, Australia

[a)] **Author to whom correspondence should be addressed:** m.meuwly@unibas.ch

ABSTRACT

The photodissociation dynamics of N_3^+ excited from its (linear) $^3\Sigma_g^-$/(bent) $^3A''$ ground to the first excited singlet and triplet states is investigated. Three-dimensional potential energy surfaces for the $^1A'$, $^1A''$, and $^3A'$ electronic states, correlating with the $^1\Delta_g$ and $^3\Pi_u$ states in linear geometry, for N_3^+ are constructed using high-level electronic structure calculations and represented as reproducing kernels. The reference *ab initio* energies are calculated at the MRCI+Q/aug-cc-pVTZ level of theory. For following the photodissociation dynamics in the excited states, rotational and vibrational distributions $P(v')$ and $P(j')$ for the N_2 product are determined from vertically excited ground state distributions. Due to the different shapes of the ground state $^3A''$ potential energy surface and the excited states, appreciable angular momentum $j' \sim 60$ is generated in diatomic fragments. The lifetimes in the excited states extend to at least 50 ps. Notably, results from sampling initial conditions from a thermal ensemble and from the Wigner distribution of the ground state wavefunction are comparable.

INTRODUCTION

Many important processes occurring in the Earth's atmosphere involve nitrogen-containing species as it is the most abundant element in the medium. Among these are charge transfer processes such as $N(^4S) + N_2^+(X^2\Sigma_g^+) \leftrightarrow N^+(^3P) + N_2(X^1\Sigma_g^+)$ that proceed via the formation of the N_3^+ radical cation. An early study utilized the complete active space self-consistent field (CASSCF) approach and multireference configuration interaction (MRCI) method to calculate vertical excitation energies and specify the collinear dissociation paths of the electronically excited states of the N_3^+ ion.[1] Given its importance in a variety of atmospheric reactions, the photodissociation dynamics of the N_3^+ ion warrants a detailed investigation.

Reactions involving N_3^+ are relevant in air plasmas at elevated temperatures. Under such conditions, N_3^+ can serve as an N^+ donor to species, such as NO, O_2, SO_2, N_2O, CO_2, or CO.[2–5] Thus, decomposition of N_3^+ into $N^+ + N_2$ is of particular relevance in view of the general reaction scheme $N_3^+ + M \rightarrow NM^+ + N_2$ with subsequent decomposition of NM^+. Species of particular importance that are formed through N^+ transfer reactions are NCO^+ ($N_3^+ + CO \rightarrow NCO^+ + N_2$) and NCO_2^+ ($N_3^+ + CO_2 \rightarrow NCO_2^+ + N_2$).[2] Furthermore, N_3^+ and N_4^+ have been suggested to be the most abundant nitrogen-containing ions in the lower atmosphere of Titan where N_3^+ drives several reactions involving CH_4, C_2H_2, or C_2H_4 through N^+ atom transfer.[6]

Photodissociation reactions are induced by the absorption of one or more photons by a chemical species, which then dissociates to form products. In a typical photolytic reaction, a reactant ABC with internal energy E_{int} absorbs a photon with energy $h\nu$ to form a transient activated complex $[ABC]^*$, which can undergo several types of primary photochemical processes followed by secondary processes. One possible outcome is the subsequent dissociation of $[ABC]^*$ into $A + [BC]^*$ where the product BC molecule is formed in a variety of excited quantum states whose population depends on the available energy and the dynamical details of the dissociation process

$$ABC \xrightarrow{h\nu} [ABC]^* \rightarrow A + [BC]*. \quad (1)$$

A dynamics study for a chemical reaction usually begins with the generation of an accurate potential energy surface (PES) for the

species. For the system of interest, one- and two-dimensional sections through the three-dimensional PESs for the ground and electronically excited states have been previously determined at different levels of theory.[1,7,8] In addition, one- and three-dimensional PESs for cyclic-N_3^+ were determined,[9–11] and the vibrational levels of up to ~2 eV were computed.[10,11] Finally, *ab initio* MD simulations for the vibrational spectra of linear and cyclic N_3^+ have been carried out.[12] These studies were concerned with the lower vibrational states on the ground state PES. However, a full-dimensional PES for the electronic ground state has only become available recently.[13]

The construction of high-dimensional PESs is a challenging problem for which machine learning-based approaches, such as neural networks or kernel-based methods, have found wide applicability in recent times.[14–17] One such method, rooted in the theory of reproducing kernel Hilbert spaces (RKHSs),[18] is suitable for obtaining reliable PESs. For this, a training set of data is generated using electronic structure calculations, which is then used to "train" the algorithm to produce a continuous surface by interpolating smoothly between the data points. Here, this "training set" constitutes the total electronic energy evaluated at various configurations using high-level electronic structure calculations. This method was utilized in previous work for the construction of an accurate PES for the ground state of N_3^+ at the multi reference configuration interaction (MRCI) level of theory.[13] A similar methodology has been followed for the construction of high quality PESs for other triatomic species, such as the [CNO] system,[19] N_3^-,[20] and NO_2.[21] In the current work, the focus is on those excited states of the N_3^+ cation, that are expected to be accessible during photoexcitation. Photodissociation reactions of the N_3^+ ion involve transitions between the $^3\Sigma_g^-$ ($^3A''$ in bent geometry) ground state and energetically accessible excited states. The $^1A'$, $^1A''$, and $^3A'$ excited states of N_3^+ are expected to play a role in dynamical processes owing to their energetic proximity to the ground state ($^3\Sigma_g^-$).

The present work is structured as follows. First, the methods are presented. Next, the quality of the PESs is discussed and the results from the dynamics simulations for photoexcitation to the $^3A'$ and the two singlet states are reported. Next, simulations starting from sampling the Wigner distribution of the ground state wavefunction are compared with the more conventional thermal initial conditions. Finally, the results are discussed and conclusions are drawn.

METHODS

First, the methods for generating and representing the potential energy surfaces are summarized. Following this, the quasi-classical trajectory (QCT) and quantum simulations for studying $N_3^+ \rightarrow N_2 + N^+$ photodissociation are described.

The N_3^+ potential energy surfaces

The three-dimensional PESs for the $^1A'$, $^1A''$, and $^3A'$ states of N_3^+ were computed at the multireference configuration interaction singles and doubles (MRCISD)[22,23]/aug-cc-pVTZ[24] level of theory with the Davidson quadruples correction[25] (MRCISD+Q) based on a CASSCF[26–29] reference wavefunction. In addition, the 2D PES at $r_{NN} = 2.25\ a_0$ (see below) for the $2^3A''$ state was determined. All electronic structure calculations were carried out using the Molpro 2019.1 program.[30,31] The active space included the full valence space, which amounts to 14 electrons in 12 valence orbitals, i.e., CASSCF(14,12). State-averaged (SA) calculations were carried out using eight states in total, including the two lowest states of each symmetry, i.e., $1^1A'$ and $2^1A'$, $1^1A''$ and $2^1A''$, $1^3A'$ and $2^3A'$, and $1^3A''$ and $2^3A''$ symmetries.

For the electronic structure calculations, the grid was defined in Jacobi coordinates (R, r, θ), whereby r is the separation between nitrogens N1 and N2, R is the distance between N3 and the center of mass of N1 and N2, and θ is the angle between $\vec{r}$ and $\vec{R}$; see Fig. 2. The grid includes distances $r \in [1.55, 4.00]\ a_0$, $R \in [1.5, 10.0]\ a_0$, and $\theta \in [0, 180°]$ from a seven-point Legendre quadrature. The products of the photodissociation reaction of N_3^+ are N_2 and N^+. Thus, the energy of the system for $E(R \rightarrow \infty, r)$ is the sum of the energies of the dissociation products. In the following, the "zero" of energy is set to this value according to $V(R, r, \theta) = E(R, r, \theta) - E(R \rightarrow \infty, r)$.

For the dynamics simulations, the energies on the grid are most conveniently represented in a way that allows for evaluation of energies and analytical gradients for arbitrary conformations. Here, a reproducing kernel Hilbert space (RKHS) representation is employed.[14,18] According to the representer theorem,[32] a function $f(\mathbf{x})$ for which values $f(\mathbf{x_i})$ are given for arguments $\mathbf{x}$ can always be approximated as a linear combination,

$$f(\mathbf{x}) \approx \widetilde{f}(\mathbf{x}) = \sum_{i=1}^{N} \alpha_i K(\mathbf{x}, \mathbf{x}_i). \tag{2}$$

Here, $K(\mathbf{x}, \mathbf{x}')$ is a kernel function and α_i are the coefficients to be determined from matrix inversion. If the inner product $\langle \phi(\mathbf{x}), \phi(\mathbf{x}') \rangle$ can be written as $K(\mathbf{x}, \mathbf{x}')$, the function is called a reproducing kernel of a Hilbert space $\mathcal{H}$.[33]

Here, reciprocal power decay kernel polynomials are used for the radial coordinates. For the R-coordinate kernel functions ($k^{[n,m]}$) with smoothness $n = 2$ and asymptotic decay $m = 4$,

$$k^{[2,4]}(x, x') = \frac{2}{15}\frac{1}{x_>^5} - \frac{2}{21}\frac{x_<}{x_>^6} \tag{3}$$

are employed, while $n = 2$ and $m = 6$ are used for the r dimension,

$$k^{[2,6]}(x, x') = \frac{1}{14}\frac{1}{x_>^7} - \frac{1}{18}\frac{x_<}{x_>^8}. \tag{4}$$

In both expressions, $x_>$ and $x_<$ are the larger and smaller values of x and x', respectively. Such a kernel smoothly decays to zero, giving the correct long-range behavior for atom–diatom-type interactions. For the angle θ, a Taylor spline kernel is used,

$$k^{[2]}(z, z') = 1 + z_< z_> + 2z_<^2 z_> - \frac{2}{3} z_<^3. \tag{5}$$

Here, $z_>$ and $z_<$ are the larger and smaller values of z and z', respectively, and z is defined as

$$z = \frac{1 - \cos\theta}{2}, \tag{6}$$

with $z \in [0, 1]$. A combination of the three one-dimensional kernels leads to

$$K(\mathbf{x}, \mathbf{x}') = k^{[2,4]}(R, R') k^{[2,6]}(r, r') k^{[2]}(z, z'), \tag{7}$$

where $\mathbf{x}, \mathbf{x}'$ are (R, r, z) and (R', r', z'), respectively. The coefficients α_i and the RKHS representation of the PES are evaluated by using a computationally efficient toolkit.[14]

The global reactive PES for each excited electronic state is constructed by smoothly connecting the three PESs for the three symmetry-equivalent reaction channels using a switching function,

$$V(\mathbf{r}) = \sum_{j=1}^{3} \omega_j(r_j) V_j(\mathbf{r}), \tag{8}$$

where the switching function ω_j has the following exponential form:

$$\omega_i(r) = \frac{e^{-(r_i/\rho_j)^2}}{\sum_{j=1}^{3} e^{-(r_j/\rho_j)^2}}. \tag{9}$$

Such a mixing using normalized weights is akin to that used in multi-surface reactive MD.[34,35] The mixing parameters ρ_j for each channel are obtained using least-squares fitting. For the ^{3}A″ ground state of N_3^+, the switching parameters are $\rho = (0.65, 0.65, 0.65)\ a_0$.[13] The root mean squared error between the two sets of data is ~0.8 kcal/mol (0.034 eV) over the entire range of reference energies considered. Similarly, reactive PESs were constructed for the ^{1}A′, ^{1}A″, and ^{3}A′ excited states. For the ^{1}A′ state, the switching parameters are $\rho = (1.0, 1.0, 1.0)\ a_0$ with an root mean square error (RMSE) of ~0.6 kcal/mol (0.026 eV). For the ^{1}A″ state, the switching parameter was $\rho = (1.03, 1.03, 1.03)\ a_0$ with an RMSE of ~0.6 kcal/mol (0.026 eV), and for the ^{3}A′ state, a switching parameter of $\rho = (0.75, 0.75, 0.75)\ a_0$ yielded an RMSE of ~0.06 kcal/mol (0.003 eV) for the global reactive PES.

Quasi-classical trajectory simulations

The QCT simulations used in the present work have been extensively described in the literature.[19,36–38] Here, Hamilton's equations of motion are solved using a fourth-order Runge–Kutta numerical method. The time step was $\Delta t = 0.05$ fs, which guarantees conservation of the total energy and angular momentum, and the mass of the nitrogen atom was $m_N = 14.003\,074$ amu.

For the photodissociation simulations, structures in the vicinity of the ^{3}A″ ground state PES and velocities were generated by drawing from a Maxwell–Boltzmann distribution at temperatures between 500 and 3000 K. At every temperature, 500 000 initial conditions were generated and propagated on the ground state PES, and the final positions and velocities were saved. The temperatures were chosen such as to bracket the zero point energy on the ^{3}A″ ground state PES, which is at 1421 cm^{-1}, corresponding to ~2000 K. For a view of the ensemble of structures, see Fig. S1. Following this, the entire population is projected vertically to the excited state PESs. Trajectories on the excited state PESs are run until dissociation into products occurs, which is defined as $R > 20\ a_0$ or for a maximum of 50 ps. Configurations initially located around the ground state minima land in the vicinity of a potential well when projected onto the ^{3}A′ PES. Subsequent trajectories are initially confined in the region around the minima before dissociating into products. Examples for photodissociating trajectories from initial velocities generated at 1000 K on the ^{3}A′ PES are shown in Fig. S2.

The product ro-vibrational states are determined following semiclassical quantization. Since the ro-vibrational states of the product diatom are continuous numbers, the states need to be assigned to integer quantum numbers for which a Gaussian binning (GB) scheme was used. For this, Gaussian weights centered around the integer values with a full width at half maximum of 0.1 were used.[38–40] It is noted that using histogram binning (HB) was found to give comparable results for a similar system.[19]

Bound vibrational states for electronically excited states of N_3^+

The vibrational energy levels supported by the singlet excited state PESs are computed using the DVR3D suite of codes.[41] For this, the nuclear time-independent Schrödinger equation is solved over a discrete grid in Jacobi coordinates (R, r, θ). In this method, the three internal coordinates are treated in a discrete variable representation (DVR). The angular coordinate is represented as a 56-point DVR based on the Gauss–Legendre quadrature, and the radial coordinates utilize a DVR based on Gauss–Laguerre quadratures with 72 points along R and 48 points along r. The angular basis functions are Legendre polynomials, and the radial basis functions are Laguerre polynomials. For the ^{3}A′ PES, the states predissociate due to the double-well structure of the surface; see Fig. 1.

For the radial degrees of freedom, a DVR[41] based on Morse-oscillator-like functions was used. The optimized Morse

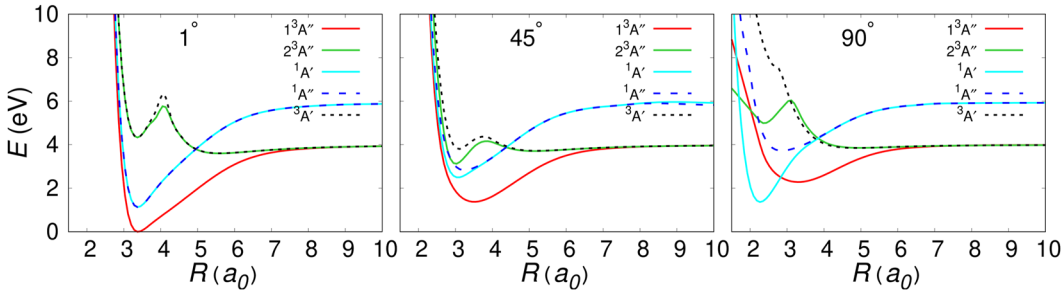

FIG. 1. One-dimensional sections of the three-dimensional PESs of the ground and excited states of N_3^+. All cuts are taken at $r = 2.25\ a_0$, and the values of the angle θ are indicated at the top of each plot. For linear N_3^+ ($\theta = 0$), the ground state (^{3}A″) correlates with the $^3\Sigma_g^-$ state, the two ^{1}A states (^{1}A′ and ^{1}A″, degenerate in linear geometry) correlate with the $^1\Sigma_g^+$ state, and ^{3}A′ and 2^3A″ correlate with the $^3\Pi_u$ state.

parameters for the grid in r for the $^1A'$ state are $r_e = 2.50\ a_0$, $D_e = 0.32\ E_h$, and $\omega_e = 0.006\ E_h$ and $R_e = 3.4\ a_0$, $D_e = 0.15\ E_h$, and $\omega_e = 0.0015\ E_h$ for R. With these parameters, the r grid for $^1A'$ extends from 1.49 to 3.46 a_0, while the R grid ranges from 1.20 to 5.51 a_0. The corresponding Morse parameters for the $^1A''$ state are $r_e = 2.45\ a_0$, $D_e = 0.32\ E_h$, and $\omega_e = 0.0065\ E_h$ along r and $R_e = 3.5\ a_0$, $D_e = 0.15\ E_h$, and $\omega_e = 0.0015\ E_h$ for R. The r grid is from 1.48 to 3.36 a_0, while the R grid spans 1.30–5.61 a_0. For the determination of the rotational levels, the body-fixed z axis is oriented along R. The corresponding vibrational wavefunctions obtained as amplitudes over a discrete grid in Jacobi coordinates are transformed to symmetric $(R_{N1N2} + R_{N2N3})/\sqrt{2}$, asymmetric $(R_{N1N2} - R_{N2N3})/\sqrt{2}$, and bending coordinates $\angle$ N1N2N3 using a Gaussian kernel-based interpolation method. Here, the triatomic is denoted as N1–N2–N3. This transformation allows for the approximate assignment of the wavefunctions using quantum numbers obtained by counting the nodal planes along each coordinate.

RESULTS

The potential energy surfaces of the excited states

In the following, the quality and topology of the excited state PESs determined in the present work are described. The $1^3A''$ ground state PES, correlating with the $^3\Sigma_g^-$ state in linear geometry and dissociating to $N^+(^3P) + N_2(X^1\Sigma_g^+)$, was already discussed in earlier work.[13] Next, up in energy are the $^1A'$ and $^1A''$ states (see the left panel of Fig. 1), which are degenerate for $\theta = 0$, correlate with the $^1\Delta_g$ state, and dissociate to $N^+(^1D) + N_2(X^1\Sigma_g^+)$. Upon bending away from the linear structure, the degeneracy is lifted and two states—$^1A'$ and $^1A''$—emerge, as is shown in the middle and right panels of Fig. 1. The overall shapes of the two PESs for the ^1A states follow that of the $^3A''$ ground state PES.

At yet higher energy and most relevant for the photodissociation dynamics considered later are the $^3A'$ and $2^3A''$ states, which

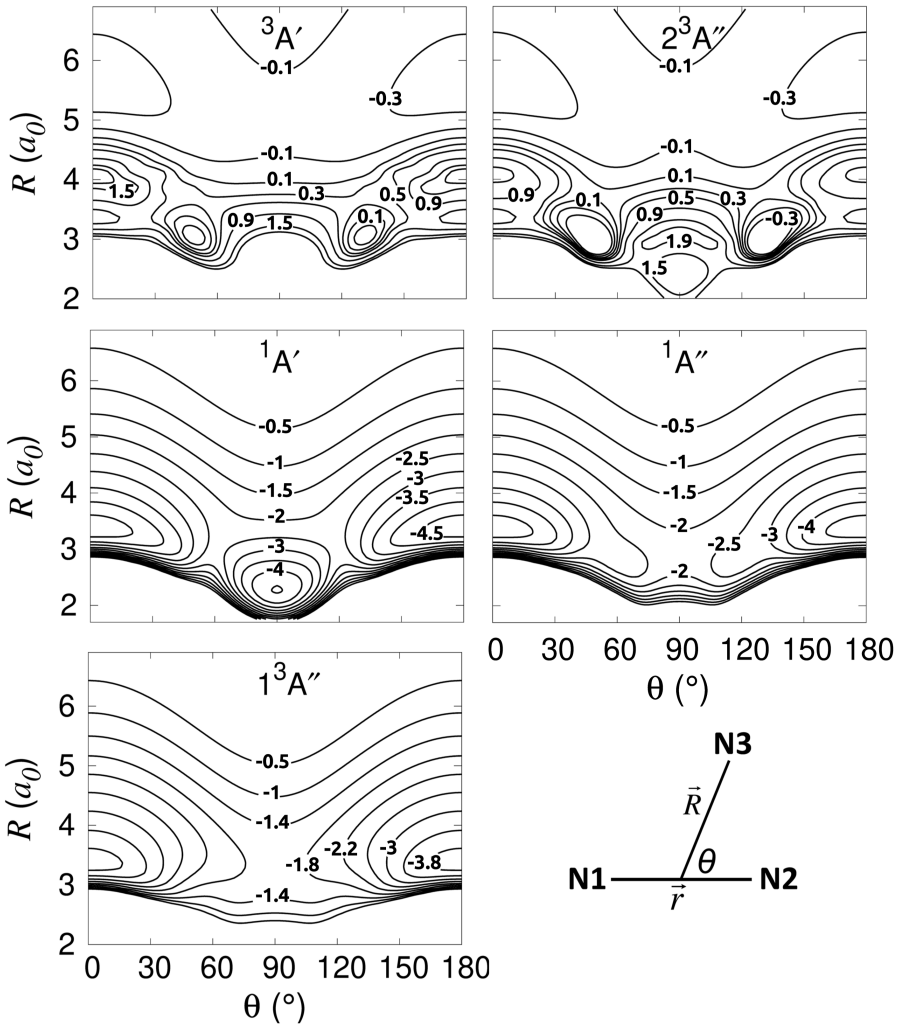

FIG. 2. Two-dimensional contour plots for the PESs of the $1^3A''$ ground state ($^3\Sigma_g^-$ for linear N_3^+, lower left panel), the two ^1A states ($^1A'$, middle left panel and $^1A''$, middle right panel) corresponding to the $^1\Delta_g$ state in the linear structure, and the two ^3A states ($^3A'$, upper left panel and $2^3A''$, upper right panel) correlating with the $^3\Pi_u$ state. In all panels, the N1–N2 diatomic separation is fixed at $r = 2.25\ a_0$. The asymptote for the triplet states is $E_{N_2} + E_{N^+(^3P)}$, and for the singlet states, it is $E_{N_2} + E_{N^+(^1D)}$. All energies are reported in eV. The bottom right panel shows the Jacobi coordinates (R, r, θ) used for describing the three-dimensional PESs for N_3^+. The vector $\vec{r}$ is the N1–N2 separation, $\vec{R}$ is the separation between N3 and the center of mass of N1–N2, and θ is the angle between the two distance vectors.

correlate with the $^3\Pi_u$ state in linear geometry. Both states dissociate to $N^+(^3P) + N_2(X^1\Sigma_g^+)$, i.e., they have the same asymptote as the $1^3A''$ ($^3\Sigma_g^-$) ground state. The $^3A'$ state has a double minimum PES with a first minimum at $R = 3.365\ a_0$, which is higher in energy than the corresponding $N_2(^1\Sigma_g^+) + N^+(^3P)$ asymptote by 0.328 eV and separated from it by a barrier of 2.351 eV in the linear configuration; see Fig. 1. This double-well structure of the PES disappears upon bending of the N_3^+ molecule and leads to a repulsive PES for a T-shaped structure; see the right-hand panel of Fig. 1. Thus, $^3\Pi_u \leftarrow {}^3\Sigma_g^-$ excitation of linear N_3^+ from the ground to the excited state is expected to lead to pronounced angular dynamics also because the structure with $\theta = 45°$ in the region of the excitation ($R \in [3, \ldots, 4]\ a_0$) is lower in energy than for the linear conformation; see the middle panel of Fig. 1. For the $2^3A''$ state, the 1D cuts resemble the $^3A'$ state for the linear and $\theta = 45°$ geometries. For the T-shaped conformation, there is a local minimum at $R = 2.384\ a_0$. For $R > 3\ a_0$, the $^3A'$ and $2^3A''$ states overlap again. Because the geometry of the $^3A''$ ground state is linear, photoexcitation to the triplet states is expected to primarily populate regions around $\theta = 0$.

The vertical excitation energies for the $^1\Delta_g \leftarrow {}^3\Sigma_g^-$ and the $^3\Pi_u \leftarrow {}^3\Sigma_g^-$ transitions have been determined or estimated from experiments.[42] For the $^1\Delta_g \leftarrow {}^3\Sigma_g^-$ transition, the excitation energy estimated from photoelectron spectroscopy is 1.13 eV, and for the $^3\Pi_u \leftarrow {}^3\Sigma_g^-$ transition, a laser spectroscopy study yielded an excitation energy of 4.54 eV.[43] From the present calculations and for the linear configuration with $r = 2.25\ a_0$, these two excitation energies are 1.13 and 4.35 eV, respectively; see Fig. 1. These results agree favorably with experiments. Earlier MRCI calculations reported transition energies of 1.30 and 4.48 eV and 1.13 and 4.28 eV when Davidson corrections are included.[1]

The RKHS representations for the four electronically excited states are provided in Fig. 2. The minimum energy structure of the $^3A''$ ground state (Fig. 2, bottom left) is 3.99 eV below the $N_2(^1\Sigma_g^+) + N^+(^3P)$ limit with a barrier of 2.28 eV for interconversion between the two equivalent linear minima. The $^3A'$ state (Fig. 2, upper left) has minima at $\theta = 49.8°(130.8°)$, 0.493 eV above the $N_2(^1\Sigma_g^+) + N^+(^3P)$ dissociation limit, and local minima at $\theta = 0°(180°)$, 0.328 eV above the same asymptote. It also contains local maxima at $\theta = 0°(180°)$ with height 2.351 eV above the same asymptote. For the $2^3A''$ state, a two-dimensional PES at fixed N1–N2 separation $r_{NN} = 2.25\ a_0$ was determined on the same (R, θ) grid as for all other states. The RKHS representation is illustrated in the upper right panel of Fig. 2. For the linear geometry $\theta = 0°$, the $^3A'$ and $2^3A''$ PESs are degenerate and associated with the $^3\Pi_u$ state (see Fig. 1), with a slight difference around $R \sim 4\ a_0$. For nonlinear geometries, the two states split as was already found in earlier electronic structure calculations.[8] Overall, the topography of the $^3A'$ and $2^3A''$ states, which both derive from the $^3\Pi_u$ state of linear N_3^+, is similar except for a local minimum in the T-shaped geometry for the $2^3A''$ state. This minimum is separated by a barrier of ~1.6 eV from the minimum at $\theta \sim 45°$. As the $^3A'$ and $2^3A''$ PESs are similar for $\theta \lesssim 45°$ and photoexcitation from the ground state primarily populates this region of the PES, the photodissociation dynamics on the $^3A'$ and $2^3A''$ surfaces are expected to be comparable. Sampling of the local minimum around $\theta \sim 90°$ on the $2^3A''$ state following photoexcitation is unlikely as this local, T-shaped minimum is separated by a barrier exceeding 1 eV from the region with $\theta \leq 45°$.

The $^1A'$ and $^1A''$ states derive from the $^1\Delta_g$ state of linear, centrosymmetric N_3^+. The $^1A'$ state (Fig. 2, middle left) has two minima, a local one at $\theta = 0°(180°)$, 4.824 eV below the $N_2(^1\Sigma_g^+) + N^+(^1D)$ asymptote, and the global one at $\theta = 90°$, which is 5.090 eV below the same asymptote. The barrier between the two minima is 2.425 eV above the respective asymptote. The $^1A''$ state (Fig. 2, middle right) features a minimum at linear positions 4.824 eV below the $N_2(^1\Sigma_g^+) + N^+(^1D)$ asymptote. The barrier between the two symmetrical minima is 2.229 eV above the respective asymptote. The locations and energies of all the critical points are summarized in Table I.

As a verification for the quality of the RKHS representation, electronic energies at additional grid points, which are not part of the training set, are evaluated from *ab initio* calculations and evaluation of the RKHS. The correlation between the reference MRCI+Q energies and their representation as a RKHS is given in Fig. 3. For the $^1A'$ state, energies at 400 additional grid points are calculated and a correlation coefficient of 0.999 69 is obtained, demonstrating the high accuracy of the RKHS-represented PESs. Similarly, validation sets of 530 and 315 grid points for the $^1A''$ and $^3A'$ states yield correlation coefficients of 0.999 98 and 0.999 78, respectively.

The crossing seams between the two singlet electronic states, which are degenerate in the linear configuration, are reported in Fig. S3. The geometries at which the two states cross were stored whenever the energy difference between the $^1A'$ and $^1A''$ states was smaller than 10^{-5} eV for a given geometry. Crossing seams are shown for three different values of the angle θ. Thus, for the excited vibrational states, there is a possibility of nonadiabatic transitions between the $^1A'$ and $^1A''$ states.

TABLE I. Minima and transition states for the three-dimensional ground and excited PESs of N_3^+ considered in the present work. The PESs are represented in Jacobi coordinates. All interatomic distances are in bohr (a_0), and angles are in degree. Energies are reported in eV with respect to the $N + N + N^+(^3P)$ asymptote for the triplet states and the $N + N + N^+(^1D)$ asymptote for the singlet states. The electronic states are labeled for both $D_{\infty h}$ and C_s symmetries. Results for the $2^3A''$ state are not reported because only a two-dimensional PES was determined.

		R	r	θ	E
$^3\Sigma_g^-/{}^3A''$	MIN1	3.38	2.25	0.0	−13.05
	MIN2	3.38	2.25	180.0	−13.05
	TS1	3.37	2.14	90.0	−10.90
$^1\Delta_g/{}^1A'$	MIN1	2.18	2.51	90.0	−14.10
	MIN2	3.38	2.25	0.0	−13.83
	MIN3	3.38	2.25	180.0	−13.83
	TS1	2.84	2.34	61.0	−11.35
	TS2	2.84	2.34	119.0	−11.35
$^1\Delta_g/{}^1A''$	MIN1	3.38	2.25	0.0	−13.83
	MIN2	3.38	2.25	180.0	−13.83
	TS1	2.97	2.18	90.0	−11.27
$^3\Pi_u/{}^3A'$	MIN1	3.01	2.41	49.2	−9.50
	MIN2	3.01	2.41	130.8	−9.50
	MIN3	3.36	2.24	0.0	−8.69
	MIN4	3.36	2.24	180.0	−8.69
	TS1	3.36	2.32	21.0	−8.51
	TS2	3.36	2.32	159.0	−8.51
	TS3	5.06	2.09	90.0	−9.56

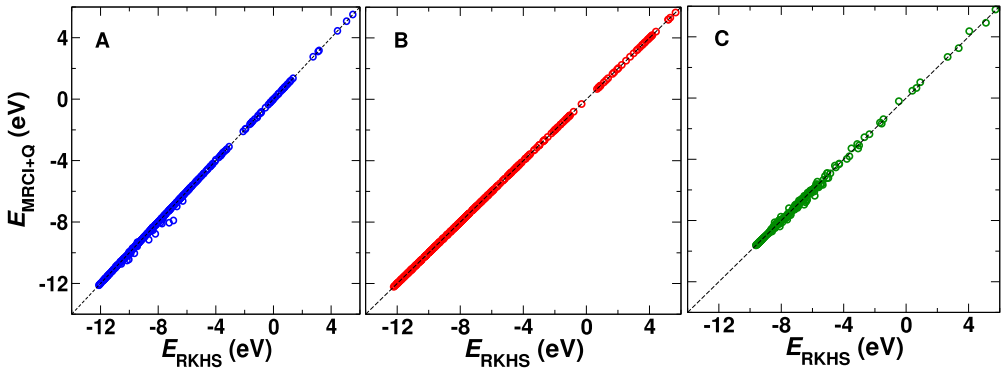

FIG. 3. Correlation between *ab initio* and RKHS energies for the $^1A'$ (a), $^1A''$ (b), and $^3A'$ (c) excited states of N_3^+. The respective correlation coefficients for the three PES are $R^2 = 0.999\,69$ for $^1A'$, $R^2 = 0.999\,98$ for $^1A''$, and $R^2 = 0.999\,78$ for the $^3A'$ state.

$^3\Pi_u \leftarrow {}^3\Sigma_g^-$ photodissociation dynamics

The photodissociation dynamics on the excited $^3A'$ state is studied by evaluating the vibrational and rotational state distributions of the products. The product final state distributions from initial conditions generated at the different temperatures are shown in Fig. 4. Vertical photoexcitation of a thermalized ensemble of molecules from the ground electronic state predominantly leads to N_2 photofragments in their ground vibrational state $v' = 0$. As temperature increases, higher v' values become populated gradually with $v'_{max} = 4$. In Fig. 4, the final rotational distributions at all temperatures are also shown. Only the results for the most populated $v' = 0$ state are presented. The excited state population is distributed over a wide range of rotational states with the peak of the distribution shifting to higher values as temperature increases. Examples for photodissociating trajectories at 1000 K on the $^3A'$ PES are shown in Fig. S2. Configurations initially located around the ground state minima land in the vicinity of a potential well when projected onto the $^3A'$ PES. Several of these trajectories are confined in the region around the minima for a few vibrational periods before dissociating into products. Several trajectories also arrive at the potential barrier near $\theta \sim 0^\circ$ and undergo dissociation immediately. Note that only trajectories resulting from initial conditions with $\theta = 0^\circ$ to 90° are shown in Fig. 4. Trajectories initialized from $\theta = 90^\circ$ to 180° follow similar dynamical paths on account of the symmetry of the PES. The distribution of lifetimes $P(\tau)$ of the N_3^+ complex in Fig. 4 indicates that a large fraction of the trajectories leads to photodissociation within 5 ps after excitation. However, there are also a number of trajectories with considerably longer lifetimes. Figure S4 shows one such trajectory at 1000 K with a lifetime of 17 ps.

Up to this point, the entire ground state population was projected onto the excited state PES and the dynamics was followed. In other words, it was assumed that the resonance condition, $h\nu = E_{photon} = E_{es} - E_{gs} = \Delta V$, is always fulfilled. Here, $h\nu$ is the energy of the incoming photon and E_{gs} and E_{es} are the energies of the molecule in the ground and excited states, respectively. However, experimentally, typically only a fraction of the population is promoted from the lower to the upper state. Such processes constitute a subset of the trajectories discussed so far and are discussed next. An examination of the PESs corresponding to $\theta \approx 0^\circ$ in Fig. 1 reveals that the difference in energies between the respective minima on the $^3A'$ and $^3A''$ states is $\Delta V \approx 4$ eV, indicating that with initial conditions in the vicinity of the ground state minimum, molecules would require ~4 eV energy for the transition to the excited state. Hence, the following different cases are considered: (1) $\Delta V > 0.15\ E_h$ (≈4 eV), (2) $\Delta V < 0.15\ E_h$, and (3) $\Delta V = 0.15 \pm 0.025\ E_h$. The results for the ensuing dynamics from trajectories sampled from initial conditions at 2000 K are shown in Fig. 4 (right-hand column). The respective distributions when all trajectories are photoexcited are also shown on the same graphs for comparison. The energy difference for case (1) corresponds to a photon wavelength of $\lambda < 310$ nm.

If only the low-energy part of the distribution is promoted to the excited state ($\Delta V < 0.15\ E_h$), the population of the vibrationally excited state in the product state is slightly smaller than for the other three cases. Conversely, excitation with $\Delta V > 0.15\ E_h$ leads to a maximum value j'_{max}, which is somewhat lower than for the remaining cases. The most pronounced differences arise for the lifetimes on the excited state, which depend on what fraction of the ground state distribution is excited. For high-energy excitation ($\Delta V > 0.15\ E_h$), lifetimes are strongly clustered on the picosecond time scales with a maximum lifetime of 20 ps. For near-resonant excitation ($\Delta V = 0.15 \pm 0.025\ E_h$), lifetimes on the several 10 ps time scale are more probable, extending out to 50 ps. Excitation of the low-energy part of the ensemble (green) leads to a higher probability for longer lifetimes, but the shape of the distribution is similar to that for exciting the entire ground state population (blue).

$^1\Delta_g \leftarrow {}^3\Sigma_g^-$ photodissociation dynamics

Formally, the $^3A' \rightarrow {}^1A'$ and $^3A' \rightarrow {}^1A''$ transitions involve a change of multiplicity and are forbidden and, therefore, less probable. Nevertheless, it is of interest to consider how the final state distributions depend on the different topographies of the underlying PESs by comparing final state distributions from transitions to the $^3A''$, $^1A'$, and $^1A''$ states, respectively; see Fig. 2.

For the linear geometry, the $^1A'$ and $^1A''$ PESs are degenerate. As shown in the middle row of Fig. 2, the most notable difference between the two singlet states is the presence of a potential well near $\theta = 90^\circ$ for the $^1A'$ state. Thus, a trajectory starting with $\theta \approx 0^\circ$

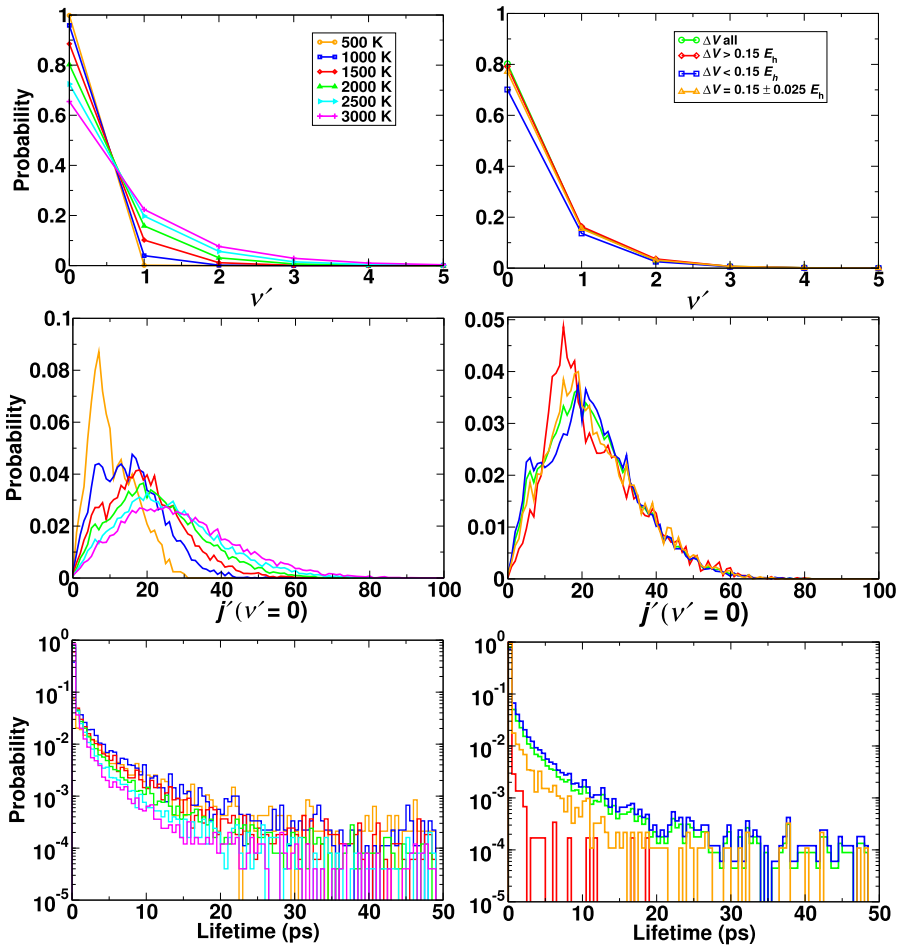

FIG. 4. Photodissociation dynamics on the ^{3}A′ PES. Left column: product vibrational (top) and rotational (middle) state distributions and lifetime distributions (bottom) from simulations started with velocities from Maxwell–Boltzmann distributions at different temperatures on the ground state PES and vertical excitation to the excited state. Right column: product vibrational and rotational state distributions and lifetime distributions from simulations started with velocities from Maxwell–Boltzmann distributions at 2000 K on the ground state PES. The analysis is carried out for different criteria for $\Delta V = V_{es} - V_{gs}$ as specified in the legend and in the text. For comparison, the product state distributions when all initial conformations undergo photoexcitation are shown in blue. In all cases, the resulting trajectories are propagated for a maximum time of 50 ps or until dissociation, whichever is earlier.

or 180° on the ^{1}A″ state remains confined in the neighborhood of the potential wells until sufficient energy has accumulated along the dissociative coordinate(s) to decompose, whereas a trajectory with similar initial conditions but propagating on the ^{1}A′ state PES may potentially travel toward $\theta = 90°$ on account of the presence of a minimum at this position. However, the barrier to reach this minimum is ~2.75 eV (see Table I), which is too high to be overcome at the conditions studied here. Nevertheless, away from the global minimum, the shapes of the two singlet PESs differ somewhat.

The final state vibrational distributions from dynamics on the ^{1}A′ PES are dominated by a population of $v' = 0$ with a maximum population of $v' = 1$ at higher temperatures only reaching ~10%; see the left column of Fig. 5. For the rotational state distributions $P(j')$ corresponding to $v' = 0$, the maxima occur between $j' = 10$ and $j' = 13$ depending on temperature. Short lifetimes (~1 ps) on the excited state PES before dissociation are about one order of magnitude more probable than lifetimes of ~50 ps at 1000 K. This changes to a difference of 2 orders of magnitudes at 3000 K with short lifetimes becoming much more probable.

For photodissociation from the ^{1}A″ state (Fig. 5, right column), an excitation of $v' = 1$ reaches up to 20% for higher temperatures. This is a clear difference compared with vibrational products dissociating from the ^{1}A′ state. For the rotational distributions corresponding to $v' = 0$, the maxima also shift progressively to higher j' values with increasing temperature, but the maxima occur at somewhat higher rotational quantum numbers compared with dissociation by populating the ^{1}A′ state. Finally, for the ^{1}A″ state at $T \sim 1000$ K, short lifetimes are about one order of magnitude more probable than long lifetimes. Short lifetimes become even more probable as temperature increases. These aspects are similar for dynamics on the ^{1}A′ state.

Overall, photodissociation on the two singlet states follows comparable patterns although details in the final state rotational distributions indicate that the anisotropy of the ^{1}A″ state PES differs somewhat from that of the ^{1}A′ PES; see the middle row of Fig. 2. Conversely, photodissociation from the ^{3}A′ state leads to more pronounced population of vibrationally excited states $v' > 0$, in particular at higher temperatures, and the rotational distributions $P(j'; v' = 0)$ appear broader with the maxima of the distributions shifted to higher values of j' compared with photodissociation from the two singlet states. This can be related to the flatter PES along the angular coordinate in the ^{3}A′ state compared with the two singlet

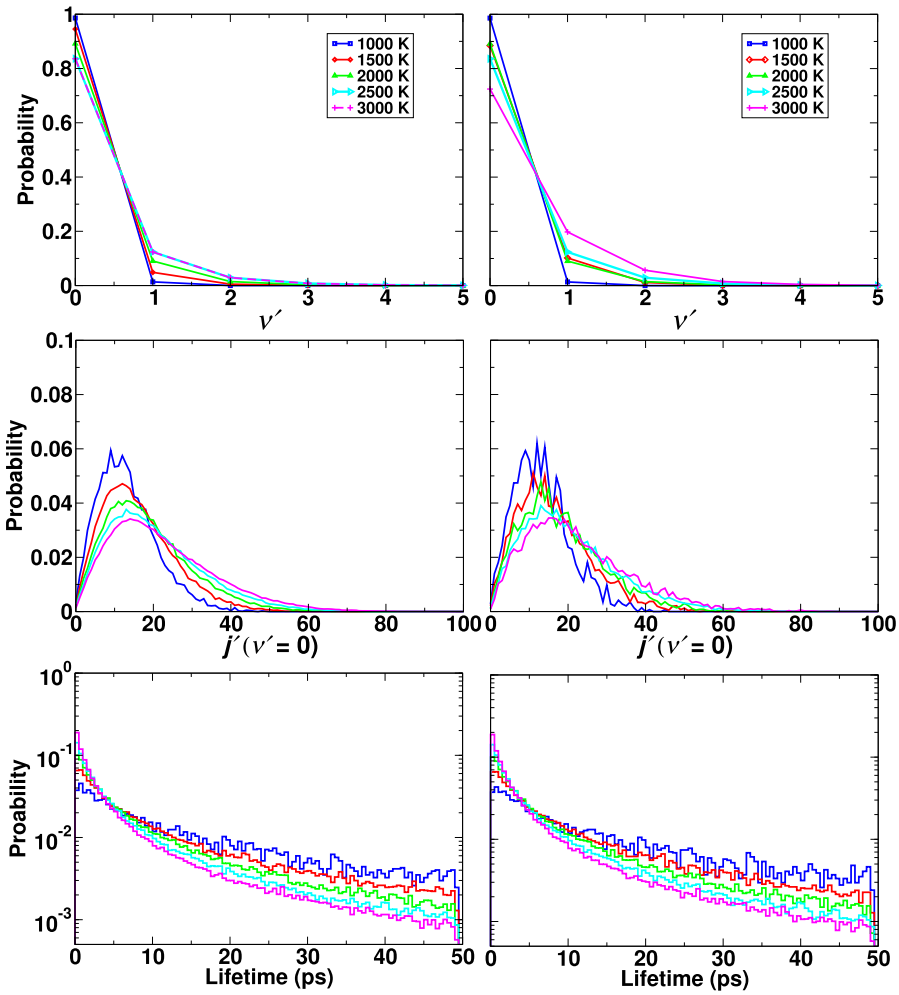

FIG. 5. Photodissociation dynamics for the singlet excited state PESs of N_3^+. Product vibrational and rotational state distributions and lifetime distributions at different temperatures for photodissociation of N_3^+ on the $^1A'$ (left column) and $^1A''$ (right column) excited states. Thermalized initial conditions are generated on the ground state at the respective temperatures and propagated on the excited state PES. In all cases, the resulting trajectories are propagated for a maximum time of 50 ps or until dissociation, whichever is earlier.

states, which leads to sampling of larger angular distortions and to increased torque upon photodissociation.

DISCUSSION AND CONCLUSION

So far, the photodissociation dynamics of the N_3^+ ion in the lowest singlet and triplet excited states was followed based on QCT simulations. Consistent with the shape differences between the $^3\Sigma_g^-$ ground state PES and the three electronically excited PESs, high rotational excitations in j' after photodissociation are found. To further corroborate this finding, simulations starting from sampling the Wigner distribution[44,45] of the $^3\Sigma_g^-$ ground state wavefunction were also carried out. The Wigner function $f_W(\Gamma)$ related to a three-dimensional wavefunction in Jacobi coordinates $\Psi(R, r, \theta)$ is given as

$$f_W(\Gamma) = (\pi\hbar)^{-3} \int ds_R ds_r ds_\theta \quad e^{2i(P_{s_R} + p_{s_r} + P_{s_\theta})/\hbar} \times \Psi^*(R + s_R, r + s_r, \theta + s_\theta) \times \Psi(R - s_R, r - s_r, \theta - s_\theta) \quad (10)$$

with $\Gamma = (R, r, \theta, P, p, P_\theta)$. Initial conditions for photodissociation are generated by sampling the probability distribution $f_W(\Gamma)$ in Eq. (10) using Metropolis Monte Carlo importance sampling. Here, $\Psi(R, r, \theta)$ is the ground state wavefunction for the $^3A''$ PES. The collection of initial conditions generated on the ground state PES in this manner represents the quantum wavepacket, which is then projected onto the excited state as before, and the dynamics is followed from QCT simulations.

The resulting final state distributions are shown in Fig. 6. The quantum ground state is 1421 cm^{-1} above the minimum energy of the PES, corresponding to 2000 K. Final state distributions from classical trajectories sampled from the Wigner distribution closely follow those from classical simulations with initial conditions at low temperature (500 K). Since "temperature" is not a meaningful physical quantity for such small systems,[46] T is rather more a label to distinguish how initial conditions were generated for ensembles, which are increasingly energized. Given this, it is encouraging to see that final state distributions from classical trajectories starting from two very different strategies to generate initial conditions are consistent with one another.

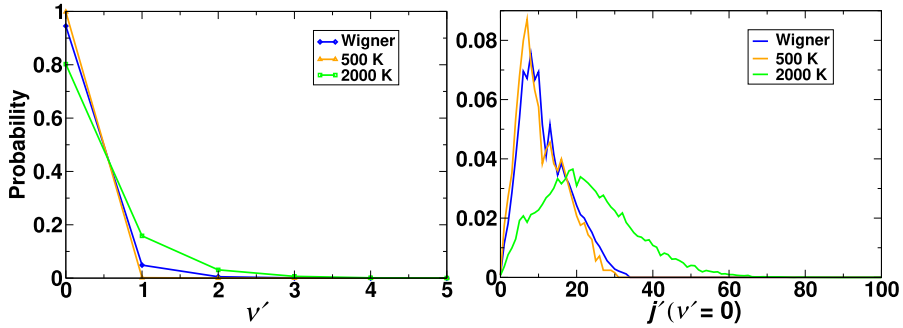

FIG. 6. Photodissociation dynamics for the ^{3}A′ excited state of N_3^+ with trajectories started from configurations obtained by sampling the Wigner distribution (blue) corresponding to the quantum ground state on the $^3\Sigma_g^-$ state and from QCT simulations at 500 K (orange) and 2000 K (green), respectively. Final vibrational (left) and rotational (right) state distributions are shown. The results are for vertical excitation from the ground to the $^3\Pi_u/^3$A′ excited state.

To corroborate the pronounced coupling of the intermolecular modes, it is also useful to consider the lower quantum bound states for the different PESs. For this, the three-dimensional time-independent Schrödinger equation was solved for the lowest bound vibrational states on the two lowest singlet electronically excited PESs, neglecting Renner–Teller coupling. The zero point vibrational energies for the ^{1}A′ and ^{1}A″ PESs are 1809 and 1707 cm^{-1}, respectively. Fundamentals are at 1019 and 1281 cm^{-1} for the v_3 antisymmetric stretch, at 1496 and 1241 cm^{-1} for the v_1 symmetric stretch, and at 1041 and 814 cm^{-1} for the v_2 bending vibration. This compares with fundamentals at 1096, 774, and 395 cm^{-1} for the v_1, v_3, and v_2 vibrations on the $^3\Sigma_g^-$ ground state PES. The higher vibrational states (combination bands and overtones) are approximately assigned using vibrational quantum numbers based on node counting; the results are reported in Table II. It must be noted that the assignments are rather approximate due to the anharmonicities and strong couplings prevalent among the vibrational levels of the excited states. This can also be seen for the representative wavefunctions for lower energy levels of the ^{1}A′ and ^{1}A″ states shown in Figs. S5 and S6, respectively. Similar calculations for the triplet state ^{3}A′ were not performed as it predissociates and requires full scattering calculations, which are outside the scope of the present work.

TABLE II. Lower bound states (in cm^{-1} above the ground state) for the singlet electronically excited states of N_3^+. The bound states are assigned to vibrational quantum numbers v_1 (symmetric stretch), v_2 (bend), and v_3 (antisymmetric stretch) by node counting; see Figs. S5 and S6, for example. The labels are only approximate due to strong coupling. The angular momentum quantum number is *l*.

$v_1 v_2^l v_3$	^{1}A′	$v_1 v_2^l v_3$	^{1}A″
0 0^0 1	1018.8	0 1^1 0	813.6
0 1^1 0	1040.9	1 0^0 0	1241.2
1 0^0 0	1496.1	0 0^0 1	1281.1
0 0^0 2	2033.1	0 2^0 0	1627.4
0 1^1 1	2048.9	1 1^1 0	2064.1
0 2^0 0	2063.3	0 1^1 1	2068.3
1 1^1 0	2490.8	0 0^0 2	2435.7
1 0^0 1	2492.7	0 3^1 0	2446.8
2 1^1 1	2512.8	2 0^0 0	2455.3
2 2^0 0	2825.9	1 0^0 1	2601.5
2 0^0 0	2979.7	0 2^0 1	2853.4
0 0^0 3	3041.1	1 2^0 0	2885.1
1 0^0 3	3481.9	2 1^1 0	3242.4

The current work investigates the photodissociation dynamics of the N_3^+ ion for the three lowest electronically excited states. For this, an ensemble of initial conditions is generated on the ground state PES and projected onto each of the excited states. For the ^{3}A′ PES, it is found that $P(v')$ essentially does not depend on how the excitation takes place. Excitation of the entire ground state population gives a similar $P(v')$ compared with near-resonant excitation or when only the high-energy part of the ground state distribution is excited. This is somewhat different for $P(j')$ for which excitation of the high-energy population yields slightly lower j'_{max} compared with the other three excitation schemes. Using initial conditions sampled from the Wigner distribution of the ground state wavefunction to initiate the dynamics on the ^{3}A′ excited state leads to comparable final state distributions $P(v')$ and $P(j')$ as do simulations started from initial conditions generated at 500 K. Product state distributions for the 2^3A″ state are expected to be similar to those from excitation to the ^{3}A′ state due to the similar shape of the PES for $\theta \leq 45°$. Even for larger bending angles, the two PESs are quite similar except for a high-lying T-shaped minimum for short *R*-separations, which is, however, energetically inaccessible.

Interpretation of experiments for the charge and atom transfer reactions for N^+ colliding with the ground state N_2 based on state correlation diagrams suggested that the $^3\Sigma^-$ and $^3\Pi$ states of N_3^+ do not interact.[47] Furthermore, a comparison of experiments with $^{14}N_2^+$ and $^{15}N^{14}N^+$ indicated that up to an energy of 6 eV above the ground state, N_3^+ behaves adiabatically. This is also consistent with computations for cyclic N_3^+.[48] Finally, spin–orbit effects were expected to be small.[47] On the other hand, it was speculated[47] that nonadiabatic coupling was strong between the $^3\Pi$ ground state and higher-lying $^3\Pi$ states not considered in the present work. These qualitative arguments suggest that for a first characterization of the photodissociation dynamics of N_3^+ involving the lowest electronically excited states, including nonadiabatic and spin–orbit effects, is not mandatory. It is, however, anticipated that including couplings between neighboring PESs in the dynamics simulations will lead to changes in the branching ratios of the photoproducts. This has, for example, been found for the [CNO] reaction system for which the ratio $k_{CO}/(k_{CO} + k_{CN})$ of the rates for CO and CN production agrees with the experiment within error bars from simulations, including nonadiabatic transitions, whereas neglecting them underestimates the ratio by about a factor of two for temperatures of up

to 1000 K.[19] For higher temperatures, the influence of nonadiabatic effects decreases, though.

In conclusion, the present work reports testable results for experiments from classical and semiclassical dynamics on accurate high-level potential energy surfaces for this important ion. It is hoped that the predictions spur experimental efforts to better characterize the photodissociation dynamics of N_3^+. This will be of particular relevance to atmospheric and interstellar chemistry.

SUPPLEMENTARY MATERIAL

See the supplementary material for the initial conditions on the ground state PES, individual photodissociating trajectories, the crossing seams between the singlet PES, and wavefunctions for the fundamentals on the two singlet PESs.

ACKNOWLEDGMENTS

Support from the Swiss National Science Foundation through Grant No. 200020_188724, the NCCR MUST (to M.M.), and the University of Basel is also acknowledged. Part of this work was supported by the United States Department of the Air Force, which is gratefully acknowledged (to M.M.). This work was supported by the Australian Research Council Discovery Project Grants (Grant Nos. DP150101427 and DP160100474). M.M. acknowledges the Department of Chemistry of Melbourne University for a Wilsmore Fellowship during which this work was initiated.

AUTHOR DECLARATIONS

Conflict of Interest

The authors have no conflicts to disclose.

DATA AVAILABILITY

All information necessary to construct the potential energy surfaces is available at https://github.com/MMunibas/N3p_PESs.

REFERENCES

[1]F. R. Bennett, J. P. Maier, G. Chambaud, and P. Rosmus, "Photodissociation, charge and atom transfer processes in electronically excited states of N_3^+," Chem. Phys. **209**, 275–280 (1996).

[2]G. De Petris, A. Cartoni, G. Angelini, O. Ursini, A. Bottoni, and M. Calvaresi, "The N_3^+ reactivity in ionized gases containing sulfur, nitrogen, and carbon oxides," ChemPhysChem **7**, 2105–2114 (2006).

[3]A. J. Midey, T. M. Miller, and A. A. Viggiano, "Reactions of N^+, N_2^+, and N_3^+ with NO from 300 to 1400 K," J. Chem. Phys. **121**, 6822–6829 (2004).

[4]D. B. Dunkin, F. C. Fehsenfeld, A. L. Schmeltekopf, and E. E. Ferguson, "Three-body association reactions of NO^+ with O_2, N_2, and CO_2," J. Chem. Phys. **54**, 3817–3822 (1971).

[5]S. Popovic, A. J. Midey, S. Williams, A. I. Fernandez, A. A. Viggiano, P. Zhang, and K. Morokuma, "Ion-molecule rate constants and branching ratios for the reaction of $N_3^+ + O_2$ from 120 to 1400 K," J. Chem. Phys. **121**, 9481–9488 (2004).

[6]V. Anicich, D. Milligan, D. Fairley, and M. McEwan, "Termolecular ion–molecule reactions in titan's atmosphere, I: Principal ions with principal neutrals," Icarus **146**, 118–124 (2000).

[7]G. Chambaud, P. Rosmus, F. Bennett, J. P. Maier, and A. Spielfiedel, "Vibrational motion in the $X^3\Sigma_g^-$ state of N_3^+," Chem. Phys. Lett. **231**, 9–12 (1994).

[8]R. Tarroni and P. Tosi, "Cyclic and bent electronic states of the N_3^+ ion," Chem. Phys. Lett. **389**, 274–278 (2004).

[9]J. J. Dillon and D. R. Yarkony, "Seams near seams: The Jahn-Teller effect in the $^1E''$ state of N_3^+," J. Chem. Phys. **126**, 124113 (2007).

[10]D. Babikov, V. A. Mozhayskiy, and A. I. Krylov, "The photoelectron spectrum of elusive cyclic-N_3 and characterization of the potential energy surface and vibrational states of the ion," J. Chem. Phys. **125**, 084306 (2006).

[11]V. a. Mozhayskiy, D. Babikov, and A. I. Krylov, "Conical and glancing Jahn-Teller intersections in the cyclic trinitrogen cation," J. Chem. Phys. **124**, 224309 (2006).

[12]F. Jolibois, L. Maron, and A. Ramírez-Solís, "*Ab initio* molecular dynamics studies on the lowest triplet and singlet potential surfaces of the azide cation: Anharmonic effects on the vibrational spectra of linear and cyclic N_3^+," J. Mol. Struct.: THEOCHEM **899**, 9–17 (2009).

[13]D. Koner, M. Schwilk, S. Patra, E. J. Bieske, and M. Meuwly, "N_3^+: Full-dimensional ground state potential energy surface, vibrational energy levels, and dynamics," J. Chem. Phys. **153**, 044302 (2020).

[14]O. T. Unke and M. Meuwly, "Toolkit for the construction of reproducing kernel-based representations of data: Application to multidimensional potential energy surfaces," J. Chem. Inf. Model. **57**, 1923–1931 (2017).

[15]S. Manzhos and T. Carrington, "Neural network potential energy surfaces for small molecules and reactions," Chem. Rev. **121**, 10187–10217 (2021).

[16]O. T. Unke, S. Chmiela, H. E. Sauceda, M. Gastegger, I. Poltavsky, K. T. Schütt, A. Tkatchenko, and K.-R. Müller, "Machine learning force fields," Chem. Rev. **121**, 10142–10186 (2021).

[17]M. Meuwly, "Machine learning for chemical reactions," Chem. Rev. **121**, 10218–10239 (2021).

[18]T. S. Ho and H. Rabitz, "A general method for constructing multidimensional molecular potential energy surfaces from *ab initio* calculations," J. Chem. Phys. **104**, 2584–2597 (1996).

[19]D. Koner, R. J. Bemish, and M. Meuwly, "The $C(^3P) + NO(X^2\Pi) \rightarrow O(^3P) + CN(X^2\Sigma^+)$, $N(^2D)/N(^4S) + CO(X^1\Sigma^+)$ reaction: Rates, branching ratios, and final states from 15 K to 20 000 K," J. Chem. Phys. **149**, 094305 (2018).

[20]S. M. Salehi, D. Koner, and M. Meuwly, "Vibrational spectroscopy of N_3^- in the gas and condensed phase," J. Phys. Chem. B **123**, 3282–3290 (2019).

[21]J. C. San Vicente Veliz, D. Koner, M. Schwilk, R. J. Bemish, and M. Meuwly, "The $N(^4S) + O_2(X^3\Sigma^-_g) \leftrightarrow O(^3P) + NO(X^2\Pi)$ reaction: Thermal and vibrational relaxation rates for the $^2A'$, $^4A'$ and $^2A''$ states," Phys. Chem. Chem. Phys. **22**, 3927–3939 (2020).

[22]H. J. Werner and P. J. Knowles, "An efficient internally contracted multiconfiguration-reference configuration interaction method," J. Chem. Phys. **89**, 5803–5814 (1988).

[23]P. J. Knowles and H.-J. Werner, "An efficient method for the evaluation of coupling coefficients in configuration interaction calculations," Chem. Phys. Lett. **145**, 514–522 (1988).

[24]T. H. Dunning, "Gaussian basis sets for use in correlated molecular calculations. I. The atoms boron through neon and hydrogen," J. Chem. Phys. **90**, 1007–1023 (1989).

[25]S. R. Langhoff and E. R. Davidson, "Configuration interaction calculations on nitrogen molecule," Int. J. Quantum Chem. **8**, 61–72 (1974).

[26]H. J. Werner and P. J. Knowles, "A second order multiconfiguration SCF procedure with optimum convergence," J. Chem. Phys. **82**, 5053–5063 (1985).

[27]P. J. Knowles and H.-J. Werner, "An efficient second-order MC SCF method for long configuration expansions," Chem. Phys. Lett. **115**, 259–267 (1985).

[28]H. J. Werner and W. Meyer, "A quadratically convergent multiconfiguration–self-consistent field method with simultaneous optimization of orbitals and CI coefficients," J. Chem. Phys. **73**, 2342–2356 (1980).

[29]D. A. Kreplin, P. J. Knowles, and H. J. Werner, "Second-order MCSCF optimization revisited. I. Improved algorithms for fast and robust second-order CASSCF convergence," J. Chem. Phys. **150**, 194106 (2019).

[30]H.-J. Werner, P. J. Knowles, G. Knizia, F. R. Manby, and M. Schütz, "Molpro: A general-purpose quantum chemistry program package," Wiley Interdiscip. Rev.: Comput. Mol. Sci. **2**, 242–253 (2012).

[31] H.-J. Werner, P. J. Knowles, G. Knizia, F. R. Manby *et al.*, MOLPRO, version 2019.1, a package of *ab initio* programs, 2019.
[32] B. Schölkopf, R. Herbrich, and A. J. Smola, "A generalized representer theorem," in *International Conference on Computational Learning Theory* (Springer, Berlin, Heidelberg, 2001), pp. 416–426.
[33] A. Berlinet and C. Thomas-Agnan, *Reproducing Kernel Hilbert Spaces in Probability and Statistics* (Springer Science & Business Media, Dordrecht, 2011).
[34] T. Nagy, J. Yosa Reyes, and M. Meuwly, "Multisurface adiabatic reactive molecular dynamics," J. Chem. Theory Comput. **10**, 1366–1375 (2014).
[35] M. H. Schmid, A. K. Das, C. R. Landis, and M. Meuwly, "Multi-state VALBOND for atomistic simulations of hypervalent molecules, metal complexes, and reactions," J. Chem. Theory Comput. **14**, 3565–3578 (2018).
[36] D. G. Truhlar and J. T. Muckerman, in *Atom–Molecule Collision Theory*, edited by R. B. Bernstein (Springer, 1979), pp. 505–566.
[37] N. E. Henriksen and F. Y. Hansen, *Theories of Molecular Reaction Dynamics* (Oxford University Press, 2011).
[38] D. Koner, L. Barrios, T. González-Lezana, and A. N. Panda, "State-to-state dynamics of the Ne + HeH^+ ($v = 0$, $j = 0$) → $NeH^+(v', j')$ + He reaction," J. Phys. Chem. A **120**, 4731–4741 (2016).
[39] L. Bonnet and J. C. Rayez, "Quasiclassical trajectory method for molecular scattering processes: Necessity of a weighted binning approach," Chem. Phys. Lett. **277**, 183–190 (1997).
[40] L. Bonnet and J.-C. Rayez, "Gaussian weighting in the quasiclassical trajectory method," Chem. Phys. Lett. **397**, 106–109 (2004).
[41] J. Tennyson, M. A. Kostin, P. Barletta, G. J. Harris, O. L. Polyansky, J. Ramanlal, and N. F. Zobov, "DVR3D: A program suite for the calculation of rotation–vibration spectra of triatomic molecules," Comput. Phys. Commun. **163**, 85–116 (2004).
[42] J. M. Dyke, N. Jonathan, A. E. Lewis, and A. Morris, "Vacuum ultraviolet photoelectron spectroscopy of transient species," Mol. Phys. **47**, 1231–1240 (1982).
[43] A. Friedmann, A. M. Soliva, S. A. Nizkorodov, E. J. Bieske, and J. P. Maier, "$A^3\Pi_u$–$X^3\Sigma_g^-$-electronic spectrum of N_3^+," J. Phys. Chem. **98**, 8896–8902 (1994).
[44] E. Wigner, "On the quantum correction for thermodynamic equilibrium," Phys. Rev. **40**, 749–759 (1932).
[45] J. Weinbub and D. K. Ferry, "Recent advances in Wigner function approaches," Appl. Phys. Rev. **5**, 041104 (2018).
[46] G. S. Boltachev and J. W. P. Schmelzer, "On the definition of temperature and its fluctuations in small systems," J. Chem. Phys. **133**, 134509 (2010).
[47] W. Freysinger, F. A. Khan, P. B. Armentrout, P. Tosi, O. Dmitriev, and D. Bassi, "Charge-transfer reaction of $^{14,15}N^+(^3P_J)$ + $N_2(^1\Sigma_g^+)$ from thermal to 100 eV. Crossed-beam and scattering-cell guided-ion beam experiments," J. Chem. Phys. **101**, 3688–3695 (1994).
[48] R. C. Fortenberry, T. J. Lee, and X. Huang, "Towards completing the cyclopropenylidene cycle: Rovibrational analysis of cyclic N_3^+, CNN, $HCNN^+$, and CNC^-," Phys. Chem. Chem. Phys. **19**, 22860–22869 (2017).